ACS APPLIED MATERIALS & INTERFACES

Research Article

www.acsami.org

Consecutive Morphology Controlling Operations for Highly Reproducible Mesostructured Perovskite Solar Cells

Yongzhen Wu,[†] Wei Chen,[†] Youfeng Yue,[†] Jian Liu,[†] Enbing Bi,[‡] Xudong Yang,*[,‡] Ashraful Islam,[†] and Liyuan Han*[,†,‡]

[†]Photovoltaic Materials Unit, National Institute for Materials Science, Sengen 1-2-1, Tsukuba, Ibaraki 305-0047, Japan

[‡]State Key Laboratory of Metal Matrix Composites, Shanghai Jiao Tong University, 800 Dong Chuan Road, Shanghai 200240, China

Supporting Information

ABSTRACT: Perovskite solar cells have shown high photovoltaic performance but suffer from low reproducibility, which is mainly caused by low uniformity of the active perovskite layer in the devices. The nonuniform perovskites further limit the fabrication of large size solar cells. In this work, we control the morphology of $CH_3NH_3PbI_3$ on a mesoporous TiO_2 substrate by employing consecutive antisolvent dripping and solvent-vapor fumigation during spin coating of the precursor solution. The solvent-vapor treatment is found to enhance the perovskite pore filling and increase the uniformity of $CH_3NH_3PbI_3$ in the porous scaffold layer but slightly decrease the uniformity of the perovskite capping layer. An additional antisolvent dripping is employed to recover the uniform perovskite capping layer. Such consecutive morphology controlling operations lead to highly uniform perovskite in both porous and capping layers. By using the optimized perovskite deposition procedure, the reproducibility of mesostructured solar cells was greatly improved such that a total of 40 devices showed an average efficiency of 15.3% with a very small standard deviation of 0.32. Moreover, a high efficiency of 14.9% was achieved on a large-size cell with a working area of 1.02 cm^2.

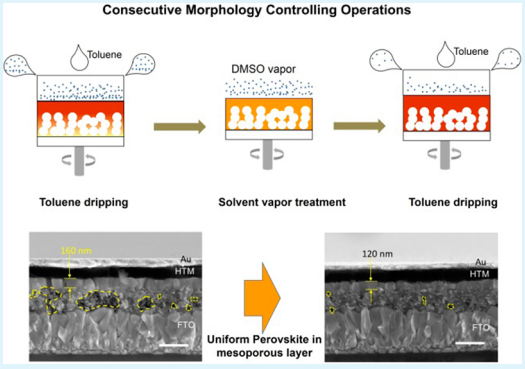

KEYWORDS: *perovskite solar cells, mesoporous, reproducibility, uniformity, solvent vapor*

INTRODUCTION

Hybrid lead halide perovskite solar cells (PeSCs) have attracted extensive recent attention because of their rapid increase of the power conversion efficiency (PCE) and potential low-cost production.[1−5] Miyasaka and co-workers first introduced perovskite as a light harvester in dye-sensitized solar cells and achieved an initial PCE of 3.8%.[6] The Snaith and Park groups independently developed solid-state PeSCs by using an organic hole-transporting material (HTM) instead of a liquid electrolyte, resulting in improved PCE and device stability.[7,8] Since then, a series of reports have demonstrated PeSC efficiency improvement, realized by either new film deposition methods or new device structures.[9−18] Seok and co-workers first proposed a "pillared structure", where perovskites in the mesoporous TiO_2 layer are densely interconnected and the HTM does not penetrate deeply into the porous TiO_2 layer.[9] The same group further optimized the perovskite deposition to realize a "bilayer structure" (Figure 1a), in which a uniform perovskite upper layer was formed on the top of the porous TiO_2 layer.[19] Up to now, the record PCE of PeSCs was achieved by using this "bilayer structure" device.[20]

Despite the rapid increase in the PCE, there are still many challenges for PeSCs, such as device reproducibility, stability, and the operation mechanism. Especially, the low reproduci-

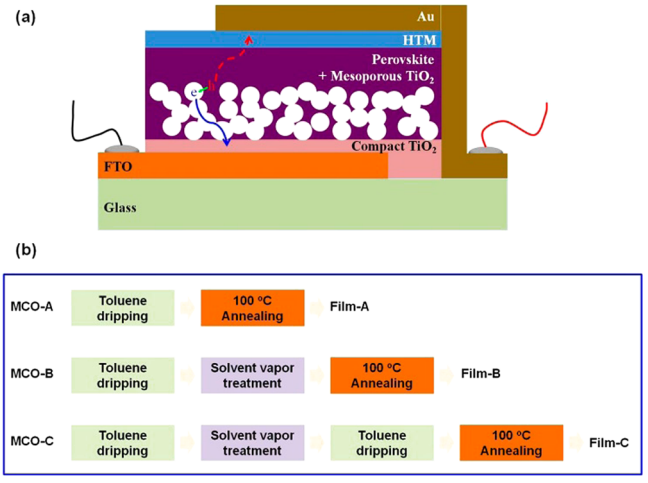

Figure 1. (a) Device architecture of mesostructured PeSCs. (b) Three kinds of MCOs applied during the fabrication of perovskite films.

Received: June 23, 2015
Accepted: August 28, 2015
Published: August 28, 2015

© 2015 American Chemical Society

DOI: 10.1021/acsami.5b05576
ACS Appl. Mater. Interfaces 2015, 7, 20707−20713

bility will hamper systematic studies and impede the fabrication of a large-size device that is necessary for accurate characterization as well as real applications. The low reproducibility of PeSCs is mainly attributed to the uncontrolled morphology of perovskites, which leads to large variations in different devices.[21,22] For "bilayer structure" devices, the perovskite in both the porous scaffold and capping layers should be uniform. Although several methods have been demonstrated to improve the perovskite coverage and decrease the surface roughness,[23−26] control of the perovskite loading in the mesoporous scaffold layer is rarely reported.

In the well-established "solvent engineering" method, "antisolvent (such as toluene) dripping" is an effective morphology controlling operation (MCO), which can induce fast precipitation of the perovskite (or intermediate) and lead to a very uniform perovskite capping layer with high surface coverage.[19,26−29] However, the precursor solution within the mesoporous scaffold does not solidify as quickly as those at the surface. Drying of the remaining precursor solution during heat treatment can lead to volume shrinkage and result in a nonuniform perovskite in the porous layer. In order to avoid or reduce volume shrinkage, there should be further diffusion of perovskite materials from the capping layer into the mesoporous scaffold after the toluene dripping operation. Because "solvent-vapor treatment" has been reported to facilitate the materials and/or ion diffusion during perovskite deposition,[11,12,30] we expect that perovskite deposition on the porous substrates may be improved by the combination of "anti-solvent dripping" and "solvent-vapor treatment".

Solvent engineering (toluene dripping) can lead to a smooth surface with full coverage, while "solvent-vapor treatment" can help perovskite material diffusion, thus affecting the morphology and crystallinity. In this work, we combine the two kinds of strategies and develop novel consecutive MCOs to improve the uniformity of $CH_3NH_3PbI_3$ in both the mesoporous scaffold and perovskite capping layers. This will improve the reproducibility of bilayer-structured PeSCs. We controlled the perovskite morphology by using consecutive MCOs during spin coating. As shown in Figure 1b, the MCOs include antisolvent (toluene) dripping, solvent-vapor fumigation, and thermal annealing. Three types of MCO combinations, i.e., MCO-A, MCO-B, and MCO-C, were designed and led to perovskite Film-A, -B, and -C, respectively. A simple toluene dripping in MCO-A can lead to a very uniform perovskite capping layer in Film-A. However, the porous layer in Film-A is less uniform because of the presence of a large amount of void areas, where the perovskite pore filling is incomplete. The solvent-vapor treatment in MCO-B was found to be capable of increasing the uniformity of perovskite in the porous layer but decreasing the uniformity of the perovskite capping layer. The additional toluene dripping in MCO-C recovers the uniformity of the perovskite capping layer, thus resulting in uniform perovskite in both the porous and capping layers. When employed in mesostructured PeSCs, Film-C-based devices showed much improved reproducibility, in which a total of 40 devices showed a high average efficiency of 15.3% with a small standard deviation of 0.32. Moreover, we further fabricate large-size devices by the optimized perovskite deposition of MCO-C, and a high efficiency of 14.9% was achieved for a cell with a working area of 1.02 cm^2.

EXPERIMENTAL METHODS

Materials and Instruments. The TiO_2 paste and spiro-OMeTAD was purchased from Dyesol and Merck, respectively. Lead iodide (Sigma-Aldrich, 99%), dimethyl sulfoxide (DMSO; Sigma-Aldrich, 99.9%), toluene (Sigma-Aldrich, 99.8%), and other commonly used reagents were used as received. CH_3NH_3I (MAI) was synthesized by following the method in the literature.[7] The scanning electron microscopy (SEM) images were taken on a JEOL JSM-6500F microscope. For top-view images, 5 mm × 5 mm samples were prepared by a glass cutter. For the cross-sectional view, the samples were cut from the back side and cracked by special pliers. Atomic force microscopy (AFM) images were taken on a JEOL JSPM 5200 microscope using noncontact scanning mode. The X-ray diffraction (XRD) patterns were collected on a Rigaku RINT-2500 powder X-ray diffractometer using Cu Kα radiation. Absorption spectra of the film samples were recorded using a Shimadzu UV/vis 3600 spectrophotometer.

Device Fabrication. Fluorine-doped tin oxide (FTO)-coated glass sheets were cut to 1.5 cm × 2.3 cm (for small cells) or 2.0 cm × 2.4 cm (for large cells) and etched with zinc powder and HCl (3 M) to obtain the desired electrode pattern. The sheets were then washed with soap, deionized water, ethanol, and acetone and finally treated under UV plasma for 30 min to remove the last traces of organic residues. A 30-nm-thick compact layer of TiO_2 was then deposited on the glass by spray pyrolysis, using a 20 mM titanium diisopropoxide bis-(acetylacetonate) solution at 500 °C. "A mesoporous TiO_2 film was spin-coated (3000 rpm for 30 s) onto the compact TiO_2/FTO substrate using Dyesol NTR-18 paste (diluted by ethanol with weight ratio of 1:4.5) and calcined at 500 °C for 2 h in air to remove organic components." The thickness of mesoporous TiO_2 was ∼300 nm. The perovskite precursor solution was prepared by mixing PbI_2 (1.20 g, 2.6 mmol) and MAI (0.41 g, 2.6 mmol) in DMSO (2 mL) and stirred at 60 °C for complete dissolution. A 70 μL perovskite solution was spread on the substrate and the spin-coating process conducted in two stages: 1000 rpm for 12 s and then 5000 rpm for 15−30 s. The time between the beginning of the 5000 rpm spin and the dripping of toluene is critical to the final film thickness as well as the cell performance. We optimized this delay time and found that 12 s is the best to start the toluene dripping. Therefore, the toluene was dripped at the 12th second from the start of the 5000 rpm spin. Usually the toluene dripping was finished within 1−2 s. In MCO-A, 0.8 mL of toluene was quickly dripped on the spinning film after high-speed rotation for 12 s, and the film was annealled at 100 °C immediately after the toluene dripping for the following annealing. In MCO-B, the toluene dripping operation is the same as that for MCO-A, and the toluene-dripped film was kept spinning in the closed spin coater for 5−10 s, followed by heat treatment. The concentration of the DMSO vapor in the spin coater was in the range of 500−1000 ppm, which was monitored by an organic solvent sensor meter (PhoCheck Tiger). MCO-C consisted of an additional toluene dripping with respect to MCO-B. The heat treatment was conducted on a hot plate at 100 °C for 10 min. After perovskite film deposition, a hole-transporting layer was deposited by spin-coating at 3000 rpm for 30 s. The spin-coating formulation was prepared by dissolving 75 mg of spiro-MeOTAD, 18 μL of 4-*tert*-butylpyridine, 37.5 mL of a stock solution of 170 mg/mL lithium bis(trifluoromethylsulfonyl)imide in acetonitrile, and 29 mL of a stock solution of 300 mg of FK102 in acetonitrile in 1 mL of chlorobenzene. Finally, 80 nm of gold was thermally evaporated on top of the device (the distance between the source and substrates was 20 cm) to form the back contact using 4.0 mm × 4.0 mm or 11.0 mm × 11.0 mm patterns. The perovskite and HTM layers were fabricated in a glovebox with O_2 and H_2O of less than 50 ppm.

Solar Cell Characterization. Current density−voltage (J−V) characteristics were recorded by applying an external potential bias to the cell while recording the generated photocurrent with a digital sourcemeter (Keithley model 2400). It was scanned from −0.2 to +1.2 V (or +1.2 to −0.2 V for the reverse scan) with a voltage step and a delay time of 10 mV and 200 ms, respectively. The light source was a 500 W class AAAAA solar simulator [Lamp Spectrum (standard A);

DOI: 10.1021/acsami.5b05576
ACS Appl. Mater. Interfaces 2015, 7, 20707−20713

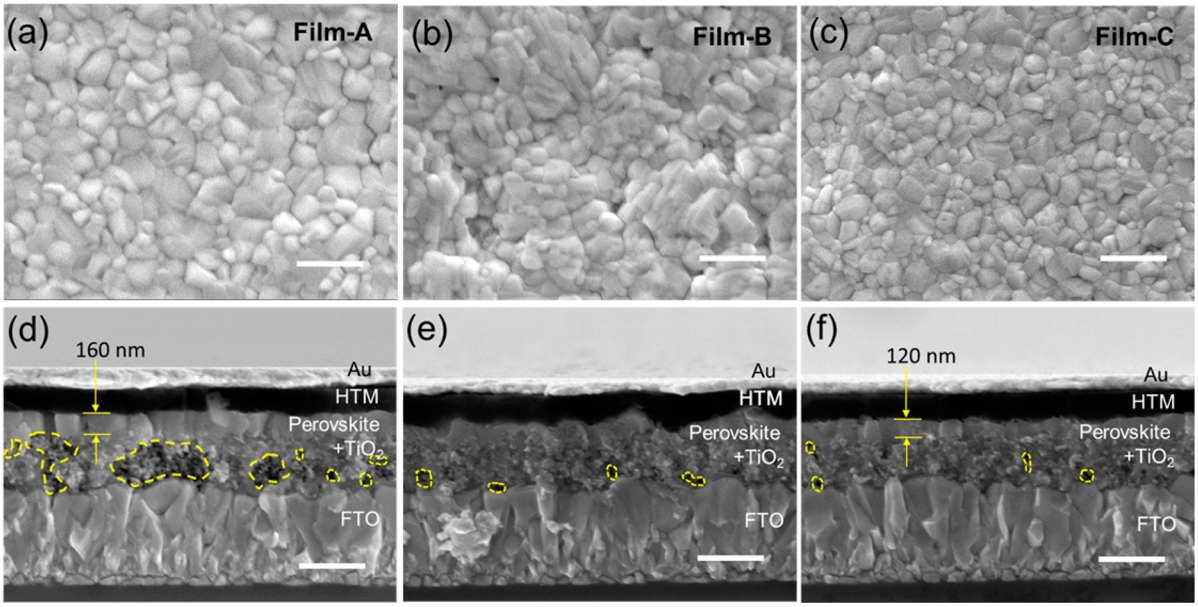

Figure 2. (a–c) Top-view SEM images of Film-A, -B, and -C. (d–f) Cross-sectional SEM images of the complete device based on Film-A, -B, and -C. Note that the white bars in parts a–f represent 500 nm.

light intensity nonuniformity, ≤±2% (A); light degree of irradiation, ≤±2% (A); test results consistency, ≤±0.5% (A); test error of the electrical properties, ≤1% (A)] equipped with an AM 1.5G filter (WXS-90L2, Wacom) at a calibrated intensity of 100 mW cm^{-2}, as determined by a standard silicon reference cell. All measurements were conducted using a nonreflective metal mask with an aperture area of 0.09 or 1.02 cm^2 to define the active area of the device and avoid light scattering through the sides.

RESULTS AND DISCUSSION

As shown in Figure 1b, MCO-A is a mimic of the reported "solvent engineering" method, which involves one-time toluene dripping during the high-speed-rotation stage of spin coating. In our experiment, we observed that the color of the spinning film turned from pale yellow to transparent brown immediately after toluene dripping. The absorption spectra of the films before and after toluene dripping were measured and compared in Figure S1 (Supporting Information), with photographs in the right panel. An increase of the absorbance in the range of 420–780 nm was observed because of toluene dripping. The profile of the absorption curve of the toluene-dripped intermediate sample is similar to the final perovskite film but with a lower absorbance value, indicating partial perovskite (or intermediate) crystallization during toluene dripping. At the moment of just finishing toluene dripping, we quickly removed this film from the spin coater to avoid the impact of solvent vapor and transferred it to a hot plate held at 100 °C for 10 min. This led to Film-A, which showed a mirrorlike reflective surface. In MCO-B, the toluene-dripped sample was not immediately taken out but kept rotating in the closed spin coater for 5–10 s. The toluene-dripped brown intermediate turned back to pale yellow during the solvent-vapor fumigation treatment. This can be rationalized by the recapture of solvent vapor, which partly breaks the as-formed rigid perovskite (or intermediate) crystal structures. Diffusion of PbI_2–MAI complexes from the capping layer into the porous layer was expected during to the solvent-vapor treatment. Film-B showed a cloudy and low-reflective surface, indicating a rougher capping layer. MCO-C contained an additional toluene dripping after the solvent-vapor treatment with respect to MCO-B. The resulting Film-C showed a surface reflection similar to that of Film-A.

The morphologies of Film-A, -B, and -C were first characterized by SEM in both the top and cross-sectional views. Figure 2a shows the top-view image of Film-A, which exhibits a smooth surface with compact grains and high coverage. From cross-sectional-view SEM images, we can also find that the perovskite capping layer of Film-A is pretty uniform, with a smooth surface and homogeneous thickness (~160 nm) across the whole film. This is consistent with the mirrorlike reflective surface observed by the naked eye. However, when we observe the cross-sectional SEM images of MCO-A-produced Film-A, void areas appear frequently in the porous layer with sizes of tens to hundreds of nanometers. Figure 2d shows one cross-sectional image of a Film-A-based solar cell, in which different sizes of void areas can be observed in the mesoporous layer, as marked by dashed yellow circles. We repeated the SEM observation with a sample number over 10 and counted the void number and size in the porous part of Film-A, as shown in Figure S2a. It can be seen that the sizes of the void areas in Film-A have a broad distribution, ranging from 50 to 300 nm. The density of small-size void areas is much higher than that of large void areas. The presence of so many void areas verified that the perovskite deposited with a simple toluene dripping shows a low uniformity in the porous layer.

The solvent-vapor treatment in MCO-B can markedly affect the morphology of the perovskite. As shown in Figure 2b, the surface of Film-B becomes not as flat as that of Film-A. It is featured with a lot of fluctuations, which accounts for the cloudy and less-reflective surface observed by the naked eye. The surface roughness (Ra) is increased from 9.19 nm for Film-A to 25.0 nm for Film-B, as measured by AFM (Figure S3). Figure 2e shows a typical cross-sectional image of the complete device using Film-B. As expected, we found that perovskite becomes more dense in the porous layer of Film-B. Compared to Film-A, both the number and size of the void areas are decreased, and the thickness of the perovskite capping layer is also decreased. The reduction of perovskite in the capping layer

DOI: 10.1021/acsami.5b05576
ACS Appl. Mater. Interfaces 2015, 7, 20707–20713

is believed to be mainly originated from perovskite transfer from the capping layer into the porous layer. After repeated observations on several batches of samples, the void numbers versus void sizes in Film-B are plotted in Figure S2b (calculated from 10 images). The porous part of Film-B only contains a few void areas with sizes of 50−100 nm. We attribute the improved uniformity of perovskite in the porous layer of Film-B to an enhanced perovskite pore filling assisted by the solvent-vapor treatment in MCO-B.

As demonstrated, the uniformity of perovskite in the porous layer was improved by the solvent-vapor treatment in MCO-B. However, it decreased the uniformity of the perovskite capping layer by increasing the surface roughness. This can be rationalized by two factors. On the one hand, the filling of void areas in the underlying porous layer will cause a subsidence in the perovskite capping layer, resulting in a thinning of the capping layer above the void areas. On the other hand, the recapture of solvent (DMSO) molecules will wet the capping layer and increase its flowability (the reason for enhanced perovskite material diffusion), and the following heat treatment will reconstruct the perovskite crystals toward surface-energy-favorable directions. This can partly counteract the effect of toluene dripping on making a smooth perovskite surface. Therefore, we introduced an additional toluene-dripping operation after the solvent-vapor treatment in MCO-C. The additional toluene dripping can recover the uniformity of the perovskite capping layer, as shown in Figure 2c. The surface morphology of Film-C is similar to that of Film-A, with a compact grain stacking and flat surface. The Ra of Film-C is 11.4 nm, as shown in Figure S3c. More importantly, as shown in Figures 2f and S2c, the high perovskite pore filling in the porous layer is maintained to that in Film-B. We speculate that the improved perovskite loading in the porous layer is caused by a concentration-gradient-induced perovskite material diffusion. After solvent-vapor treatment, the capping layer becomes an supersaturated solution, in which the perovskite concentration is much higher than that in the mesoporous scaffold. The increased flowability assists more perovskite material diffusion and results in an increase in the perovskite loading in the porous layer. Compared to Film-A, the capping layer thickness of Film-C decreased to 120 nm, further indicating that the consecutive solvent-vapor treatment and toluene-dripping operation transfer more perovskite from the capping layer into the porous layer and generate more uniform perovskite in both the porous and capping layers.

Figure 3a shows the absorption spectra of Film-A, -B, and -C. The band-edge absorption of the three films is almost the same, indicating that the total loading amounts of perovskite are almost the same for the three types of deposition procedures. This means that the DMSO-vapor treatment as well as the second-time toluene dripping does not decrease the amount of perovskite on the substrate, although they were spun for a prolonged duration. This is because, after the first toluene dripping, the surface of the film is solidified, which leads to negligible perovskite material (PbI_2 and MAI) loss in the following spinning. Accordingly, the decrease of the perovskite capping layer thickness in Film-B and -C should be attributed to more perovskite penetrating into the mesoporous layer, further proving the solvent-vapor-assisted perovskite pore filling. Figure 3b shows the XRD patterns of Film-A, -B, and -C. All three films show similar XRD patterns with a series of characteristic peaks (such as 2θ of 14.08° and 28.42°) corresponding to the tetragonal perovskite structure.[31]

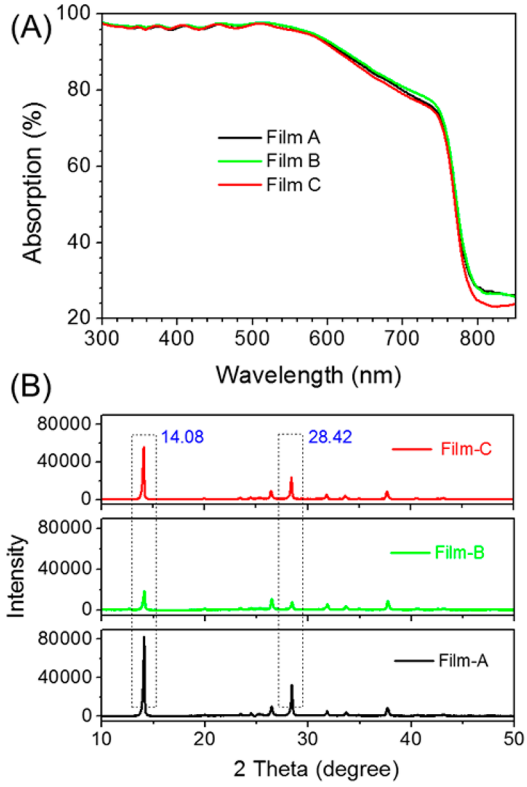

Figure 3. (a) Single-path absorption spectra of Film-A, -B, and -C measured by an integration sphere. (b) XRD patterns of Film-A, -B, and -C on a glass/FTO/mesoporous TiO_2 substrate.

However, there is a large difference in the intensity of these peaks. Taking the peaks at 14.08° as an example, Film-A, -B, and -C show peak intensities of 83000, 19000, and 56000, respectively. The full widths at half-maximum of the peak at 14.8° were estimated to be 0.13, 0.20, and 0.14 for Film-A, -B, and -C, respectively. These results indicate that different deposition methods result in different perovskite crystallinities. Because the crystal size of perovskite in mesopores is much smaller than that of perovskite in the capping layer, the decreased XRD intensity is consistent with increased perovskite located in the mesopores, namely, increasing the perovskite pore filling. The recovery of the peak intensity in XRD of Film-C suggests that the second-time toluene dripping can increase the crystallinity and/or crystal size of the perovskite in the capping layer. The intensity ratios between peaks at 14.08° and 28.42° for the three samples were calculated to be 2.55, 2.28, and 2.39 for Film-A, -B, and -C, respectively. It seems that the intensity ratio is decreased after the solvent-vapor treatment. This might be rationalized as the fact the "solvent vapor treatment" leads to more perovskite entering the porous layer, where the perovskite crystals have orientations different from those of the crystals in the capping layer. Another reason may be that the relative amount of perovskite in the porous and capping layers has changed after the "solvent-vapor treatment", thus affecting the intensity ratios of peaks at 14.08° and 28.42°.

In order to examine the effect of the three types of perovskite deposition on the photovoltaic performance, three groups (A, B, and C, with 40 cells for each group) of mesoporous-structured PeSCs were constructed using Film-A, -B, and -C in the assembly of FTO-coated glass/compact TiO_2/mesoporous TiO_2/$CH_3NH_3PbI_3$/spiro-OMeTAD/Au, respectively. Except for the perovskite deposition, the other layers were prepared

DOI: 10.1021/acsami.5b05576
ACS Appl. Mater. Interfaces 2015, 7, 20707−20713

with the same procedure and similar conditions. When stored in humidity-controlled (relative humidity RH < 10%) desiccators, the devices are relatively stable and their performances maintained 80−90% after 1 month. PeSCs usually exhibit a large discrepancy in the $J-V$ measurement when the cell is scanned with different directions and rates.[32−34] For these cells, we found that the PCE difference between the forward and reverse scans can be minimized to less than 1% by employing a relatively slow sweep rate (Figure S4). Here, we compared the results measured by the forward scan from −0.2 to +1.2 V with a voltage step of 10 mV and a delay time of 200 ms. A black metal mask with an aperture area of 0.09 cm^2 was used to define the sizes of the solar cells. The efficiency distributions of the three groups of devices are shown in Figure 4a. Although the maximum PCE of the three groups of cells can achieve over 15%, the average efficiency of group C (15.3%) is much higher than that of group B (13.8%) and group A (12.7%). Moreover, the standard deviation of the efficiency for group C (0.32) is much smaller than those of groups A (1.53) and B (0.99). Both the average efficiency and standard deviation data reveal that the reproducibility of group C is greatly improved with respect to groups A and B. Considering the same TiO_2 and HTM layers as those used for the three groups of devices, we can conclude that the improved reproducibility of group C is related to the improved uniformity of the perovskite in Film-C.

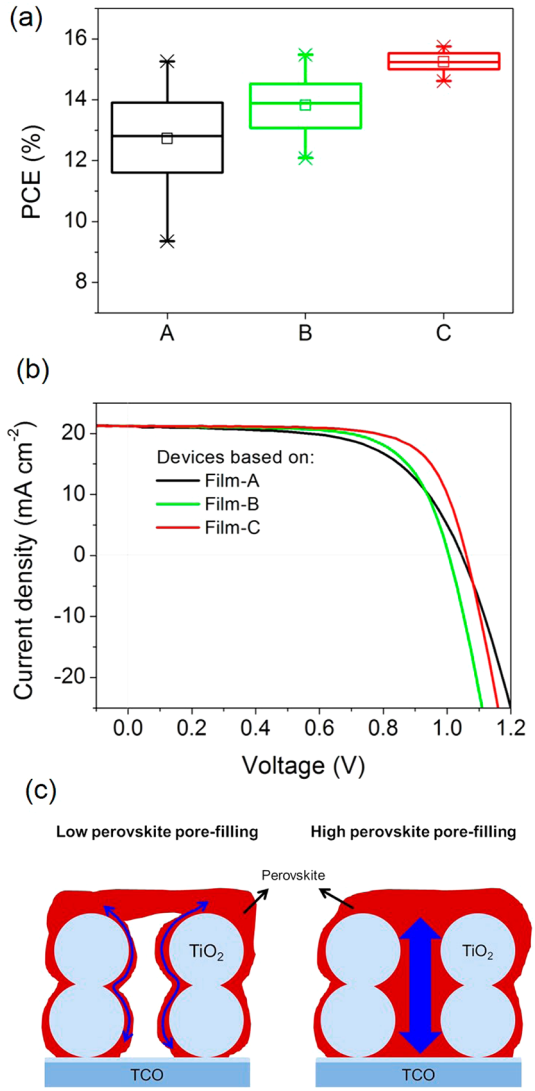

Figure 4. (a) Statistical analysis of the PCE of PeSCs processed using Film-A, -B, and -C. (b) Comparison of the forward scan $J-V$ curves of solar cells based on perovskite Film-A, -B, and -C. (c) Schematic diagram of the impact of perovskite pore filling on charge transport in the porous layer (the blue arrows indicate the charge-transport channels in perovskite).

In order to understand how the perovsktie morphology affects the reproducibility of mesoporous-structured PeSCs, we carefully examined the short-circuit current density (J_{sc}), open-circuit voltage (V_{oc}), and fill factor (FF) parameters of the above three groups of devices and plotted their distributions in Figure S5. We find that FF of devices in group A varied in a large range from 0.54 to 0.70, which is the main reason for the large deviation of their PCEs. For devices in group B, the variation of FF is decreased and the average value of FF is increased. However, their V_{oc} performance decreased and showed a slightly larger distribution. In comparison, all of the J_{sc}, V_{oc}, and FF parameters for devices in group C are highly reproducible. Figure 4b shows the typical $J-V$ curves of PeSCs based on perovskite Film-A, -B, and -C. The selected devices showed PCEs close to the average level of their corresponding groups. It can be seen that they showed very similar J_{sc} values. The FF values extracted from the three $J-V$ curves are 0.55, 0.63, and 0.67 for cells based on Film-A, -B, and -C, respectively. Obviously, the relatively low FF of a Film-A-based cell should be mainly attributed to a relatively large series resistance (R_s) because its $J-V$ curve near the V_{oc} point shows a smaller slope. The data of "series resistance" were directly obtained from the $I-V$ testing software "$I-V$ tester". We compared the PCE from relatively slow and forward scans (from −0.2 to +1.2 V), and the "series resistance" data were also taken from these forward $I-V$ scans. The deduced R_s value from the $J-V$ curves is 13.08 Ω cm^2 for a Film-A-based cell, which is much large than that of Film-B (5.99 Ω cm^2) and -C-based (5.36 Ω cm^2) devices. Here, the decreased R_s and increased FF in devices based on Film-B and -C should be attributed to denser perovskite in the mesoporous scaffold layer. For mesoscopic solar cells, the pore filling of guest materials in a mesoporous scaffold is crucial to the device performance because it influences the charge transport and recombination to a large extent. Taking the solid-state dye-sensitized solar cells as an example, the pore filling of HTM is a key point for ensuring high charge collection efficiency. In mesoscopic PeSCs, especially for the case in which perovskite forms a capping layer, the HTM forms only a covering layer above the perovskite capping layer with little HTM penetration in the porous layer. The perovskite itself is responsible for hole conduction in the whole mesoporous layer. As illustrated above, the simple toluene-dripping-based Film-A contains a lot of void areas in the porous layer due to the fast surface-initiated crystallization, while "solvent-vapor treatment" in Film-B and -C shows more compact stacking in the porous layer. Figure 4c illustrates the effect of perovskite pore filling caused by different deposition methods on charge transport. In the low-perovskite pore-filling void areas, there is only a thin perovskite layer or some isolated perovskite dots on the TiO_2 nanoparticles in the void areas. The very thin perovskite coating layer (as sketched in Figure 4c) in the void areas may not only increase the charge-transport resistance but also enhance the charge recombination.[35−37] In contrast, a high perovskite pore filling can provide a high-speed channel for charge percolation. The existence of a large number of size-variable void areas in the

DOI: 10.1021/acsami.5b05576
ACS Appl. Mater. Interfaces 2015, 7, 20707−20713

porous layer of Film-A will undoubtedly affect R_s and result in variable performances for different devices. When the open-circuit voltage (V_{oc}) performances of these devices are compared, we find that the average V_{oc} of a Film-B-based device is slightly lower than that of cells based on Film-A and C. This is probably caused by the nonuniform perovskite capping layer of the former. The presence of more nanoscaled pinholes in the capping layer of Film-B (Figure 2b) will increase the possibility of contact between spiro-OMeTAD and TiO_2, which has been identified as the major reason for V_{oc} loss in mesoporous TiO_2-based PeSCs.[38] Moreover, the fluctuated perovskite capping layer will lead to a nonuniform thickness of the HTM layer. The varied pinhole density in the perovskite capping layer and variable HTM thickness across the device should be responsible for the relatively low reproducibility of Film-B-based devices in group B. In MCO-C-produced Film-C, the uniformity of perovskite in both the porous and capping layers was improved, thus resulting in improved performance and reproducibility of devices in group C.

Considering the highly uniform perovskite films generated by MCO-C that can produce reproducible device performance, we attempt to use this technique for fabricating large-size PeSCs, which is essential for future real applications. The fabrication procedure of large-size devices is almost the same as that of the above-mentioned small-size devices in group C except for using a larger substrate and a new pattern for gold electrode evaporation. Figure 5 shows the $J-V$ curves and incident photon-to-current conversion efficiency (IPCE) spectra of large-size devices based on MCO-C-produced perovskite Film-C. Impressively, the uniform perovskite enabled a high PCE of 14.9% for a cell with a working area of 1.02 cm^2. As far as we know, these are the best results of PeSCs with active areas larger than 1 cm^2.

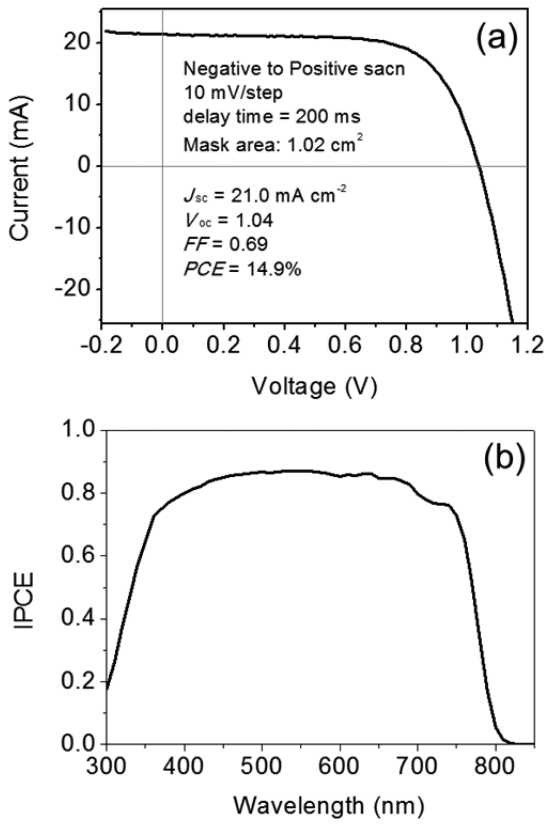

Figure 5. $J-V$ curves (a) and IPCE spectra (b) of large-size solar cells with a working area of 1.02 cm^2 based on MCO-C-produced perovskite.

CONCLUSIONS

In summary, by employing a set of consecutive MCOs, we successfully improved the uniformity of perovskite in both the porous and capping layers. For the first time, a solvent-vapor treatment is proposed for improving the uniformity of perovskite in a mesoporous layer via enhancing the perovskite diffusion. The improved uniformity of perovskite results in a significent enhancement of the performance and reproducibility of mesostructured PeSCs. A total of 40 cells based on the optimized perovskite fabrication conditions showed an average efficiency of 15.3% and a small standard deviation of 0.32. Moreover, a high efficiency of 14.9% was achieved on a large-size cell with a working area of 1.02 cm^2. The strategy of solvent-vapor-assisted perovskite loading as well as consecutive MCOs is universally useful for perovskite deposition on mesoporous-based substrates.

ASSOCIATED CONTENT

Supporting Information

The Supporting Information is available free of charge on the ACS Publications website at DOI: 10.1021/acsami.5b05576.

Supporting Figures S1–S5 (PDF)

AUTHOR INFORMATION

Corresponding Authors

*E-mail: Yang.xudong@sjtu.edu.cn.

*E-mail: Han.Liyuan@nims.go.jp. Tel: +81 298592747. Fax: +81 298592304.

Notes

The authors declare no competing financial interest.

ACKNOWLEDGMENTS

This work was financially supported by Core Research for Evolutional Science and Technology (CREST) of the Japan Science and Technology Agency.

REFERENCES

(1) Park, N. Perovskite Solar Cells: an Emerging Photovoltaic Technology. *Mater. Today* **2015**, *18*, 65–72.

(2) Gao, P.; Gratzel, M.; Nazeeruddin, M. K. Organohalide Lead Perovskites for Photovoltaic Applications. *Energy Environ. Sci.* **2014**, *7*, 2448–2463.

(3) Snaith, H. J. Perovskites: The Emergence of a New Era for Low-Cost, High-Efficiency Solar Cells. *J. Phys. Chem. Lett.* **2013**, *4*, 3623–3630.

(4) Zhou, H.; Chen, Q.; Li, G.; Luo, S.; Song, T.; Duan, H.; Hong, Z.; You, J.; Liu, Y.; Yang, Y. Interface Engineering of Highly Efficient Perovskite Solar Cells. *Science* **2014**, *345*, 542–546.

(5) Liu, X. D.; Yu, H.; Yan, L.; Dong, Q. Q.; Wan, Q.; Zhou, Y.; Song, B.; Li, Y. F. Triple Cathode Buffer Layers Composed of PCBM, C60, and LiF for High-Performance Planar Perovskite Solar Cells. *ACS Appl. Mater. Interfaces* **2015**, *7*, 6230–6237.

(6) Kojima, A.; Teshima, K.; Shirai, Y.; Miyasaka, T. Organometal Halide Perovskites as Visible-Light Sensitizers for Photovoltaic Cells. *J. Am. Chem. Soc.* **2009**, *131*, 6050–6051.

(7) Lee, M. M.; Teuscher, J.; Miyasaka, T.; Murakami, T. N.; Snaith, H. J. Efficient Hybrid Solar Cells Based on Meso-Superstructured Organometal Halide Perovskites. *Science* **2012**, *338*, 643–647.

(8) Kim, H.; Lee, C.; Im, J.; Lee, K.; Moehl, T.; Marchioro, A.; Moon, S.; Humphry-Baker, R.; Yum, J.; Moser, J. E.; Grätzel, M.; Park, N.

DOI: 10.1021/acsami.5b05576
ACS Appl. Mater. Interfaces 2015, 7, 20707–20713

Lead Iodide Perovskite Sensitized All-Solid-State Submicron Thin Film Mesoscopic Solar Cell with Efficiency Exceeding 9%. *Sci. Rep.* **2012**, *2*, 591.
(9) Heo, J. H.; Im, S. H.; Noh, J. H.; Mandal, T. N.; Lim, C.; Chang, J. A.; Lee, Y. H.; Kim, H.; Sarkar, A.; Nazeeruddin, Md. K.; Grätzel, M.; Seok, S. I. Efficient Inorganic-Organic Hybrid Heterojunction Solar Cells Containing Perovskite Compound and Polymeric Hole Conductors. *Nat. Photonics* **2013**, *7*, 486−491.
(10) Burschka, J.; Pellet, N.; Moon, S.; Humphry-Baker, R.; Gao, P.; Nazeeruddin, M. K.; Grätzel, M. Sequential Deposition as a Route to High-Performance Perovskite-Sensitized Solar Cells. *Nature* **2013**, *499*, 316−319.
(11) Chen, Q.; Zhou, H.; Hong, Z.; Luo, S.; Duan, H.; Wang, H.; Liu, Y.; Li, G.; Yang, Y. Planar Heterojunction Perovskite Solar Cells via Vapor-Assisted Solution Process. *J. Am. Chem. Soc.* **2014**, *136*, 622−625.
(12) Xiao, Z.; Dong, Q.; Bi, C.; Shao, Y.; Yuan, Y.; Huang, J. Solvent Annealing of Perovskite-Induced Crystal Growth for Photovoltaic-Device Efficiency Enhancement. *Adv. Mater.* **2014**, *26*, 6503−6509.
(13) Zhu, Z.; Bai, Y.; Zhang, T.; Liu, Z.; Long, X.; Wei, Z.; Wang, Z.; Zhang, L.; Wang, J.; Yan, F.; Yang, S. High-Performance Hole-Extraction Layer of Sol-Gel-Processed NiO Nanocrystals for Inverted Planar Perovskite Solar Cells. *Angew. Chem., Int. Ed.* **2014**, *53*, 12571−12575.
(14) Chen, W.; Wu, Y.; Liu, J.; Qin, C.; Yang, X.; Islam, A.; Cheng, Y.; Han, L. Hybrid Interfacial Layer Leads to Solid Performance Improvement of Inverted Perovskite Solar Cells. *Energy Environ. Sci.* **2015**, *8*, 629−640.
(15) Etgar, L.; Gao, P.; Xue, Z.; Peng, Q.; Chandiran, A. K.; Liu, B.; Nazeeruddin, M. K.; Grätzel, M. Mesoscopic $CH_3NH_3PbI_3/TiO_2$ Heterojunction Solar Cells. *J. Am. Chem. Soc.* **2012**, *134*, 17396−17399.
(16) Mei, A.; Li, X.; Liu, L.; Ku, Z.; Liu, T.; Rong, Y.; Xu, M.; Hu, M.; Chen, J.; Yang, Y.; Grätzel, M.; Han, H. A Hole-Conductor-Free, Fully Printable Mesoscopic Perovskite Solar Cell with High Stability. *Science* **2014**, *345*, 295−298.
(17) Qin, P.; Tanaka, S.; Ito, S.; Tetreault, N.; Manabe, K.; Nishino, H.; Nazeeruddin, M. K.; Grätzel, M. Inorganic Hole Conductor-Based Lead Halide Perovskite Solar Cells with 12.4% Conversion Efficiency. *Nat. Commun.* **2014**, *5*, 4834.
(18) You, J.; Hong, Z.; Yang, Y. M.; Chen, Q.; Cai, M.; Song, T.; Chen, C.; Lu, S.; Liu, Y.; Zhou, H.; Yang, Y. Low-Temperature Solution-Processed Perovskite Solar Cells with High Efficiency and Flexibility. *ACS Nano* **2014**, *8*, 1674−1680.
(19) Jeon, N. J.; Noh, J. H.; Kim, Y. C.; Yang, W. S.; Ryu, S.; Seok, S. I. Solvent Engineering for High-Performance Inorganic-Organic Hybrid Perovskite Solar Cells. *Nat. Mater.* **2014**, *13*, 897−903.
(20) Jeon, N. J.; Noh, J. H.; Yang, W. S.; Kim, Y. C.; Ryu, S.; Seo, J.; Seok, S. I. Compositional Engineering of Perovskite Materials for High-Performance Solar Cells. *Nature* **2015**, *517*, 476−480.
(21) Wakamiya, A.; Endo, M.; Sasamori, T.; Tokitoh, N.; Ogomi, Y.; Hayase, S.; Murata, Y. Reproducible Fabrication of Efficient Perovskite-based Solar Cells: X-ray Crystallographic Studies on the Formation of $CH_3NH_3PbI_3$ Layers. *Chem. Lett.* **2014**, *43*, 711−713.
(22) Conings, B.; Baeten, L.; De Dobbelaere, C.; D'Haen, J.; Manca, J.; Boyen, H. Perovskite-Based Hybrid Solar Cells Exceeding 10% Efficiency with High Reproducibility Using a Thin Film Sandwich Approach. *Adv. Mater.* **2014**, *26*, 2041−2046.
(23) Jeon, Y.; Lee, S.; Kang, R.; Kim, J.; Yeo, J.; Lee, S.; Kim, S.; Yun, J.; Kim, D. Planar Heterojunction Perovskite Solar Cells with Superior Reproducibility. *Sci. Rep.* **2014**, *4*, 6953.
(24) Wu, Y.; Islam, A.; Yang, X.; Qin, C.; Liu, J.; Zhang, K.; Peng, W.; Han, L. Retarding the Crystallization of PbI_2 for Highly Reproducible Planar-Structured Perovskite Solar Cells via Sequential Deposition. *Energy Environ. Sci.* **2014**, *7*, 2934−2938.
(25) Marinova, N.; Tress, W.; Humphry-Baker, R.; Dar, M. I.; Bojinov, V.; Zakeeruddin, S. M.; Nazeeruddin, M. K.; Grätzel, M. Light Harvesting and Charge Recombination in $CH_3NH_3PbI_3$ Perovskite Solar Cells Studied by Hole Transport Layer Thickness Variation. *ACS Nano* **2015**, *9*, 4200−4209.
(26) Xiao, M.; Huang, F.; Huang, W.; Dkhissi, Y.; Zhu, Y.; Etheridge, J.; Gray-Weale, A.; Bach, U.; Cheng, Y.; Spiccia, L. A Fast Deposition-Crystallization Procedure for Highly Efficient Lead Iodide Perovskite Thin-Film Solar Cells. *Angew. Chem., Int. Ed.* **2014**, *53*, 9898−9903.
(27) Jung, J. W.; Williams, S. T.; Jen, A. K. Y. Low-Temperature Processed High-Performance Flexible Perovskite Solar Cells via Rationally Optimized Solvent Washing Treatments. *RSC Adv.* **2014**, *4*, 62971−62977.
(28) Zhou, Y.; Yang, M.; Wu, W.; Vasiliev, A. L.; Zhu, K.; Padture, N. P. Room-Temperature Crystallization of Hybrid-Perovskite Thin Films via Solvent-Solvent Extraction for High-Performance Solar Cells. *J. Mater. Chem. A* **2015**, *3*, 8178−8184.
(29) Jin, Y.; Chumanov, G. Fabrication of Lead Halide Perovskite Film by Controlling Reactivity at Room Temperature in Mixed Solvents. *Chem. Lett.* **2014**, *43*, 1722−1724.
(30) Zhu, W.; Yu, T.; Li, F.; Bao, C.; Gao, H.; Yi, Y.; Yang, J.; Fu, G.; Zhou, X.; Zou, Z. A Facile, Solvent Vapor-Fumigation-Induced, Self-Repair Recrystallization of CH3NH3PbI3 Films for High-Performance Perovskite Solar Cells. *Nanoscale* **2015**, *7*, 5427−5434.
(31) Baikie, T.; Fang, Y.; Kadro, J. M.; Schreyer, M.; Wei, F.; Mhaisalkar, S. G.; Grätzel, M.; White, T. J. Synthesis and Crystal Chemistry of the Hybrid Perovskite $(CH_3NH_3)PbI_3$ for Solid-State Sensitized Solar Cell Applications. *J. Mater. Chem. A* **2013**, *1*, 5628−5641.
(32) Unger, E. L.; Hoke, E. T.; Bailie, C. D.; Nguyen, W. H.; Bowring, A. R.; Heumuller, T.; Christoforo, M. G.; McGehee, M. D. Hysteresis and Transient Behavior in Current-Voltage Measurements of Hybrid-Perovskite Absorber Solar Cells. *Energy Environ. Sci.* **2014**, *7*, 3690−3698.
(33) Tress, W.; Marinova, N.; Moehl, T.; Zakeeruddin, S. M.; Nazeeruddin, M. K.; Gratzel, M. Understanding the Rate-Dependent J-V Hysteresis, Slow Time Component, and Aging in $CH_3NH_3PbI_3$ Perovskite Solar Cells: the Role of a Compensated Electric Field. *Energy Environ. Sci.* **2015**, *8*, 995−1004.
(34) Christians, J. A.; Manser, J. S.; Kamat, P. V. Best Practices in Perovskite Solar Cell Efficiency Measurements. Avoiding the Error of Making Bad Cells Look Good. *J. Phys. Chem. Lett.* **2015**, *6*, 852−857.
(35) Stamplecoskie, K. G.; Manser, J. S.; Kamat, P. V. Dual Nature of the Excited State in Organic-Inorganic Lead Halide Perovskites. *Energy Environ. Sci.* **2015**, *8*, 208−215.
(36) Roiati, V.; Colella, S.; Lerario, G.; De Marco, L.; Rizzo, A.; Listorti, A.; Gigli, G. Investigating Charge Dynamics in Halide Perovskite-Sensitized Mesostructured Solar Cells. *Energy Environ. Sci.* **2014**, *7*, 1889−1894.
(37) Xiao, Z.; Yuan, Y.; Shao, Y.; Wang, Q.; Dong, Q.; Bi, C.; Sharma, P.; Gruverman, A.; Huang, J. Giant Switchable Photovoltaic Effect in Organometal Trihalide Perovskite Devices. *Nat. Mater.* **2014**, *14*, 193−198.
(38) Leijtens, T.; Lauber, B.; Eperon, G. E.; Stranks, S. D.; Snaith, H. J. The Importance of Perovskite Pore Filling in Organometal Mixed Halide Sensitized TiO_2-Based Solar Cells. *J. Phys. Chem. Lett.* **2014**, *5*, 1096−1102.

DOI: 10.1021/acsami.5b05576
ACS Appl. Mater. Interfaces 2015, 7, 20707−20713